Electronic Supplementary Material (ESI) for Materials Chemistry Frontiers.

Supporting Information

Breaking scaling relations in nitrogen reduction with asymmetrical heterobimetallic FeCo sites to boost ammonia synthesis

Na Xu,[a,b,‡] Yanzheng He,[a,‡] Mengfan Wang,[a,*] Chen Cheng,[a] Qiyang Cheng,[a] Sisi Liu,[a] Haoqing Ji,[a,*] Chenglin Yan,[a,c] Federico Rosei[b,d,*]

[a]College of Energy, Soochow University, Suzhou 215006, China
[b]Institut national de la recherche scientifique,1650 Boul. Lionel-Boulet, Varennes, QC J3X1P7, Canada
[c]School of Petrochemical Engineering, Changzhou University, Changzhou 213164, China
[d]Department of Chemical and Pharmaceutical Sciences, University of Trieste, Via Giorgeri 1, Trieste 34127, Italy
[‡]These authors contributed equally to this work.

Methods

DFT computational method and model. The first-principles calculations were conducted using the Vienna *ab initio* simulation package (VASP). The Perdew-Burke-Ernzerhof with generalized gradient approximation (GGA) was adopted to describe the electron-electron interaction. An energy cutoff of 450 eV was used, and a k-point sampling set of 3 × 3 × 1 was tested to be converged. The corresponding cell parameters are a = 14.760 Å, b = 14.760 Å, and c = 16.000 Å; $\alpha = 90°$, $\beta = 90°$, and $\gamma = 120°$. The criterion for all structural optimizations was set to 10^{-5} eV for electronic energy convergence and the Hellmann-Feynman force less than 0.01 eV $Å^{-1}$ for ionic relaxation loop. The vacuum space along the z-direction is set to be 15 Å. The Hubbard U correction was also employed within the DFT+U approach in all spin polarized calculations. The van der Waals dispersion forces were included using the zero damping DFT-D3 method of Grimme. The implicit solvent model, VASPsol, was applied to considered effects between the solute and solvent on the activation energies. The adsorption energy ΔE of the A group on the surface of the substrates was defined as:

$$E_{ads} = E_{*+intermediate} - E_{*} - E_{molecule} \tag{1}$$

where $E_{*+intermediate}$ and E_{*} are the energies of the surface with and without adsorbed molecules, respectively, and the $E_{molecule}$ is the energy of the molecule in the gas phase. The Gibbs free energy change (ΔG) of each chemical reaction is calculated as follows:

$$\Delta G = \Delta E - T\Delta S + \Delta ZPE + \Delta G_{pH} \tag{2}$$

where ΔE is the total energy difference between reactants and products in a specific step, ΔZPE is the zero-point energy correction, and ΔS is the entropy change in the reaction step. Here, T was set as room temperature (298.15 K). ΔG_{pH} is the contribution of H^+ and is equal to $-k_BT \times \ln(10) \times pH$, where k_B is Boltzmann's constant.

Synthesis of FeCoNC. To prepare FeCoNC, 2 ml pyrrole was adequately dispersed in deionized water by ultrasonic vibration. Excess ferrous chloride, cobalt chloride, and hydrogen peroxide were added, and the reaction lasted several hours until a bright yellow and transparent solution was obtained. Sodium chloride, zinc chloride, and silicon dioxide was further dissolved in the solution to be used as a template. The product was collected by freezedrying to obtain brown powders. The material was then placed in a ceramic boat and carbonized at 700 °C for 2 h under argon protection. The carbonized material was firstly washed with hydrofluoric acid to remove the silicon dioxide. Then, after removing the salt templates through sufficient washing with a lot of water and ethanol, the products were dried in a vacuum at 60 °C overnight to obtain black powders.

Synthesis of FeNC. To prepare FeNC, 2 ml pyrrole was adequately dispersed in deionized water by ultrasonic vibration. Excess ferrous chloride and hydrogen peroxide were added, and the reaction lasted several hours until a bright yellow and transparent solution was obtained. Sodium chloride, zinc chloride, and silicon dioxide was further dissolved in the solution to be used as a template. The product was collected by freezedrying to obtain brown powders. The material was then placed in a ceramic boat and carbonized at 700 °C for 2 h under argon protection. The carbonized material was firstly washed with hydrofluoric acid to remove the silicon dioxide. Then, after removing the salt templates through sufficient washing with a lot of water and ethanol, the products were dried in a vacuum at 60 °C overnight prior to use.

Physical characterization. The morphology was investigated by a field emission scanning electron microscopy (FESEM, SU8010, Japan) and a field emission transmission electron microscopy (FETEM, FEI Tecnai G2 F20 S-TWIN TMP, Hong Kong). The dispersion of single Fe and Co atoms was characterized by atomic resolution high-angle annular dark-field scanning transmission electron microscopy on a JEOL JEM-ARM200F instrument equipped with a probe spherical aberration corrector. The catalyst was characterized by X-ray diffraction (XRD, D8 Advance, Bruker) and Raman spectroscopy (HR evolution, Horiba Jobin Yvon, France). The XANES and the EXAFS spectra were obtained at 1W1B station in Beijing Synchrotron Radiation Facility (BSRF). The storage rings of BSRF were operated at 2.5 GeV with a maximum current of 250 mA. The data collection was carried out in transmission mode using Si (111) double-crystal monochromator, ionization chamber for Fe foil, Co foil and in fluorescence excitation mode using a Lytle detector for FeCoNC. N_2 adsorption analysis was performed by an ASAP 2020 accelerated surface area and porosimetry instrument (Micromeritics) equipped with an automated surface area, using BET to calculate the surface area at 77 K.

Nitrogen purification. The $^{14}N_2$ commercially purchased from Messer Gas Product Co., Ltd. (Germany) and $^{15}N_2$ commercially purchased from Newradar Special Gas Co., Ltd. (China) were sequentially flowed through acid (0.1 M HCl), oxidising (0.1 M $KMnO_4$), and alkaline traps (0.1 M KOH) to remove possible contaminants, including NH_3, NO, and NO_2. Then, the gas was passed through a drying tube to prevent water vapour from entering the electrochemical cell. To examine whether the gases have been sufficiently purified, the purified gases were analyzed using spectrophotometric method.

Detection of NH_3 in purified gas. To ensure that no NH_3 remains in the purified gas, the gas is passed into ultrapure water at a flow rate of 50 standard cubic cm per min (sccm) for 1 h. The obtained solution was analyzed using the indophenol blue method with some improvements. Specifically, 2 ml of 1 M sodium hydroxide solution containing sodium citrate and salicylic acid were mixed with 2 ml of treated water. Then, 1 ml of 0.05 M sodium hypochlorite solution and 0.2 ml of 1 wt.% sodium nitroferricyanide were added into the solution. The above mixture was shaken well and left to stand in the darkness for 2 hours, then the UV-vis absorption spectrum was measured. The absorbance at 655 nm was used to determine the concentration of indophenol blue. Ultrapure water was used as a blank (zero) for the baseline. The concentration-absorbance curves were calibrated using a standard ammonium chloride solution with a series of concentrations in H_2O.

Detection of NO_x contamination in purified gas. NO and NO_2 can be converted into NO_2^- and NO_3^- and captured once passing through the oxidising and alkaline traps. NO_2^- was determined by Griess spectrophotometric method. The test gas was fed into 50 ml gas absorption solution with 30 sccm for 1 hour. 0.5 g sulfanilic acid was dissolved in a mixture of 5 ml acetic acid and 90 ml H_2O. Then, 5 mg N-(1-naphthyl)-ethylenediamine dihydrochloride was added and the solution was filled to 100 ml to obtain chromogenic agent. 4 ml chromogenic agent were added into the 1 ml gas absorption solution. After further standing for 15 min, the UV-vis absorption spectrum was measured at 540 nm. The concentration-absorbance curves were calibrated using standard sodium nitrite solution with a series of concentrations in H_2O. NO_3^- was determined by sulfamic acid method. In detail, the test gas was fed into 50 ml gas absorption solution with 30 sccm for 1 hour. 0.1 ml 1 M HCl and 0.01 ml 0.8 wt.% sulfamic acid solution were added into the gas absorption solution. The absorption spectrum was recorded using an UV-vis spectrophotometer. The final absorbance value was calculated by this equation: $A = A_{220\ \mathrm{nm}} - 2A_{275\ \mathrm{nm}}$. The concentration-absorbance curves were calibrated using standard sodium nitrate solution with a series of concentrations in H_2O.

Cathode preparation. First, 1 mg of catalyst was dispersed in 980 μl of ethanol, to which 20 μl of Nafion solution (5 wt.%) was added and sonicated for one hour. The mixed solution was used as homogeneous ink. Then, 50 μl of ink was evenly coated on the carbon paper over an area of $1 \times 1\ \mathrm{cm}^2$ and dried at 80 °C for three hours. The obtained electrode was used for electrochemical measurements.

Electrochemical NRR measurements. The reduction of N_2 gas was carried out at room temperature in a two-chamber cell which was separated by a Celgard membrane with hydrophilic treatment. A three-electrode system was used for electrochemical measurements, with a carbon rod as the counter electrode and Ag/AgCl (4 M KCl) as the reference electrode. All measured potentials are converted to standard potentials versus RHE by calibration. Purified N_2 was continuously fed into the cathode section at a certain flow rate through a suitable sprayer, ensuring that the entire working electrode is in full contact with N_2 gas bubbles during the experiment. Electrochemical NRR reactions were carried out in N_2-saturated 0.1 M HCl at ambient temperature and pressure. The potentiostatic tests were carried at different potentials including -0.1, -0.2, -0.3, -0.4, -0.5 V vs. RHE.

Detection of the produced ammonia. For the colorimetric method, the produced ammonia in the 0.1 M HCl electrolyte was detected using the same method as that in water, except the ultrapure water was replaced with 0.1 M HCl. For quantitative ^{1}H NMR measurements, various concentrations of ammonium sulfate were used to prepare the standard curve. The electrolyte was removed after electrolysis at -0.2 V vs. RHE. Then, the solution was concentrated to 0.5 ml and was mixed with 0.1 ml of dimethylsulfoxide-d6. Maleic acid was used as the internal standard. The produced ammonia was quantified by using ^{1}H NMR spectroscopy (Agilent 600 MHz).

Detection of the produced hydrazine. The concentration of the produced hydrazine in the 0.1 M HCl was tested by the Watt and Chrisp method. The solution formed by the mixture of ethanol (300 ml), HCl (concentrated, 30 ml), and p-dimethylaminobenzaldehyde (5.99 g) was used as the coloring agent. 5 ml of the above coloring agent was added into 5 ml of the reacted electrolyte and mixed well by stirring. Its absorbance was measured at a wavelength of 455 nm. Standard hydrazine monohydrate solutions at a series of concentrations in 0.1 M HCl was prepared to build the calibration curves and quantify the produced hydrazine.

Determination of hydrogen evolution. The H_2 was manual sampling and analyzed by gas chromatography (GC-2014, Shimadzu).

Faradaic efficiency and the yield rate. The Faradaic efficiency and yield rate of NH_3 were calculated as follows:

$$\text{Faradaic efficiency } (\mathrm{NH_3}) = [3F \times c(\mathrm{NH_3}) \times V] / Q \tag{3}$$

$$\text{Yield rate } (\mathrm{NH_3}) = [17c(\mathrm{NH_3}) \times V] / (t \times m) \tag{4}$$

where F is the Faraday constant (96,485 C mol^{-1}), t is the electrolysis time (1 h), m is the loading mass of the catalysts, Q is the total charge passed through the electrode, V is the volume of the electrolyte, and $c(NH_3)$ is the measured ammonia concentration.

The Faradaic efficiency of H_2 was calculated as below:

$$\text{Faradaic efficiency } (\mathrm{H_2}) = [2 \times V_j \times P \times V \times 10^{-3} / RT] / [I_{total} \times t_H / F] \tag{5}$$

where V_j is volume percentage obtained from the GC analysis of H_2, P is the atmospheric pressure (101.325 KPa), R is the gas constant (8.314 J mol^{-1} K^{-1}), V is the volume of sampling loop (1 cm^3), T is the temperature in Kelvin (298.15 K), I_{total} is the recording current, and t_H is the time required to fill the sampling loop.

^{15}N isotopic labeling experiment. Purified $^{15}N_2$ was used as the feeding gas in the labeling experiments. After the electrolytic reaction, the obtained $^{15}NH_4^+$-contained electrolyte was collected. The generated $^{15}NH_3$ was quantified either by colorimetric method or ^{1}H NMR measurements (Agilent 600 MHz, USA) as that for $^{14}NH_3$.

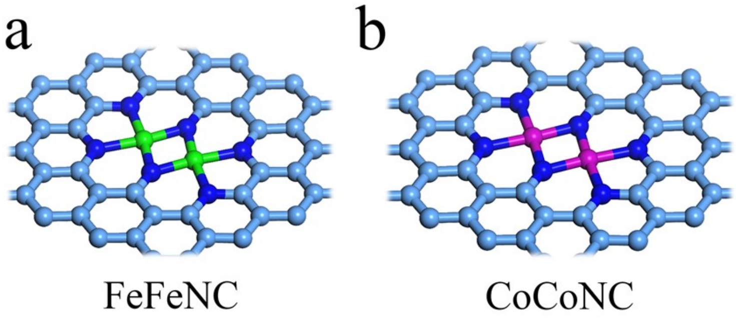

Fig. S1. Configurations of (a) FeFeNC and (b) CoCoNC.

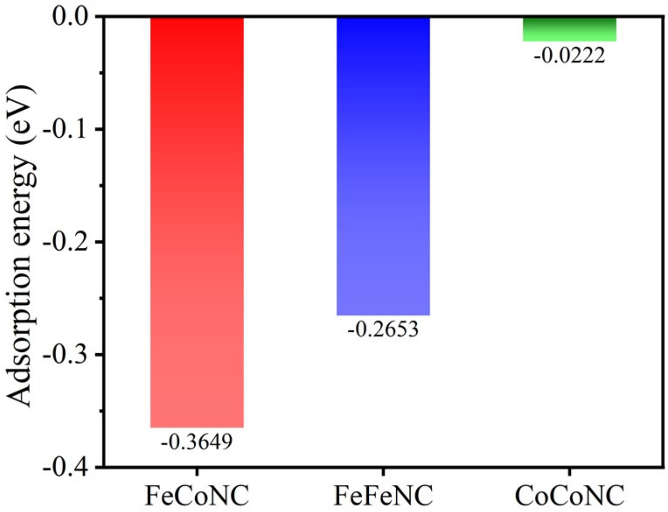

Fig. S2. Comparison of N_2 adsorption energy on the corresponding configurations.

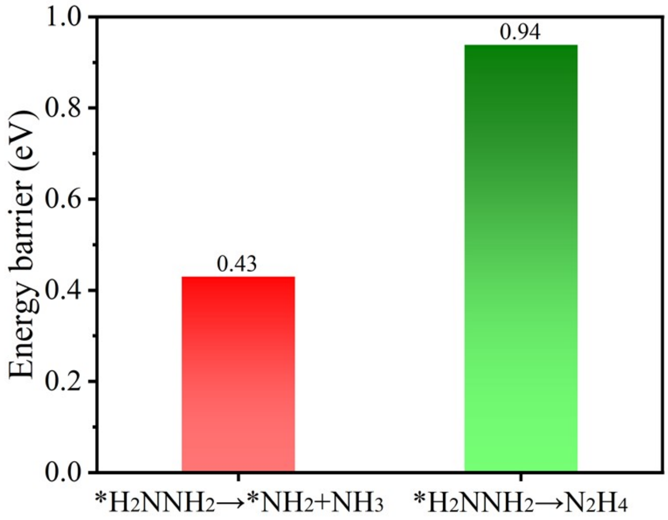

Fig. S3. The comparison of ΔG value of $*NH_2+NH_3$ and N_2H_4 generated from $*H_2NNH_2$.

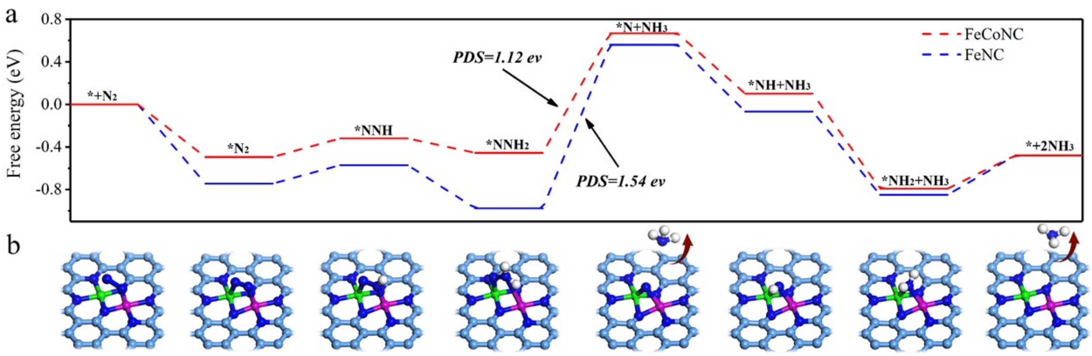

Fig. S4. (a) Free energy of ammonia synthesis on FeCoNC and FeNC through the distal pathway and (b) the corresponding configurations of adsorbates on FeCoNC. The light blue, blue, green, pink, and white spheres represent C, N, Fe, Co, and H atoms, respectively.

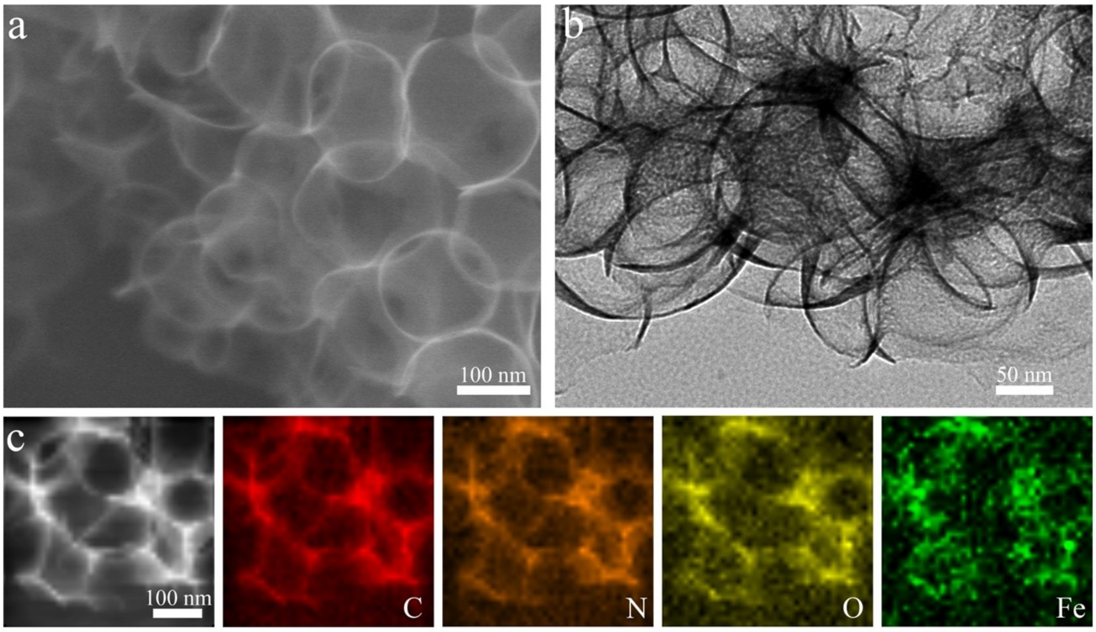

Fig. S5. (a) Scanning electron microscopy image, (b) transmission electron microscopy image, and (c) element mappings of FeNC.

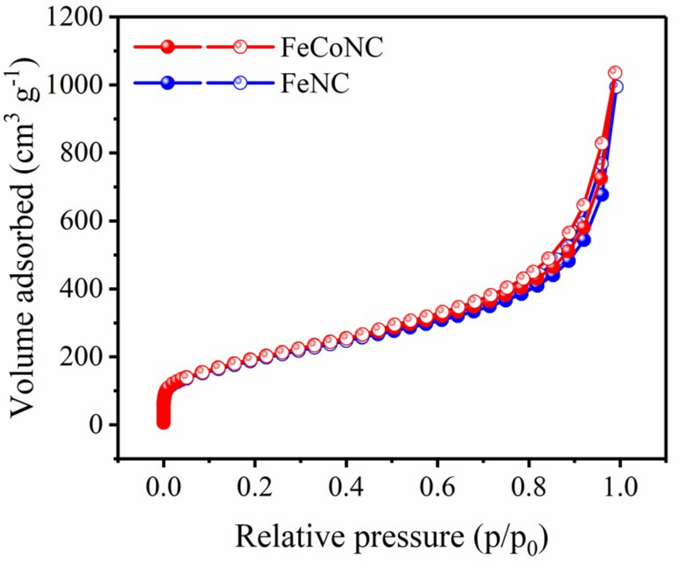

Fig. S6. N_2 sorption isotherms of FeCoNC and FeNC.

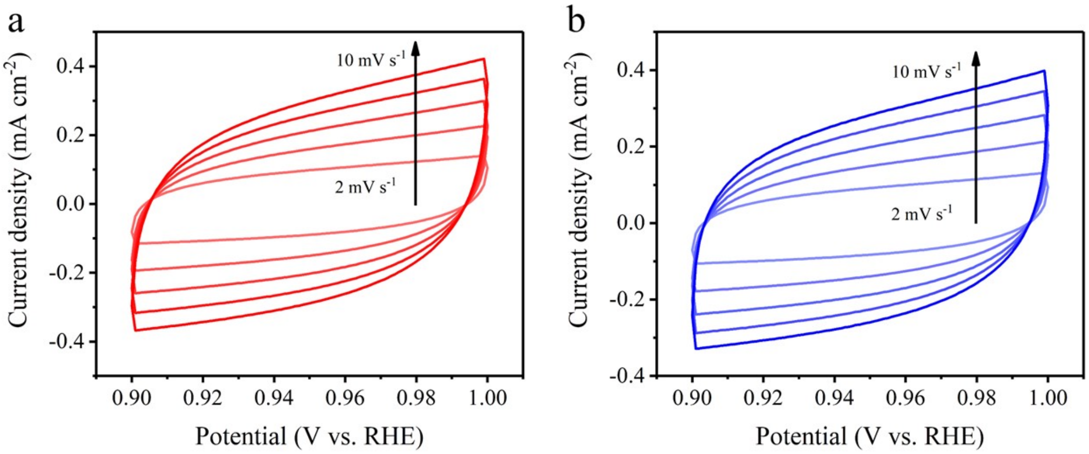

Fig. S7. Cyclic voltammograms of (a) FeCoNC and (b) FeNC taken at different scan rates in a potential window where only double-layer charging and discharging occurs.

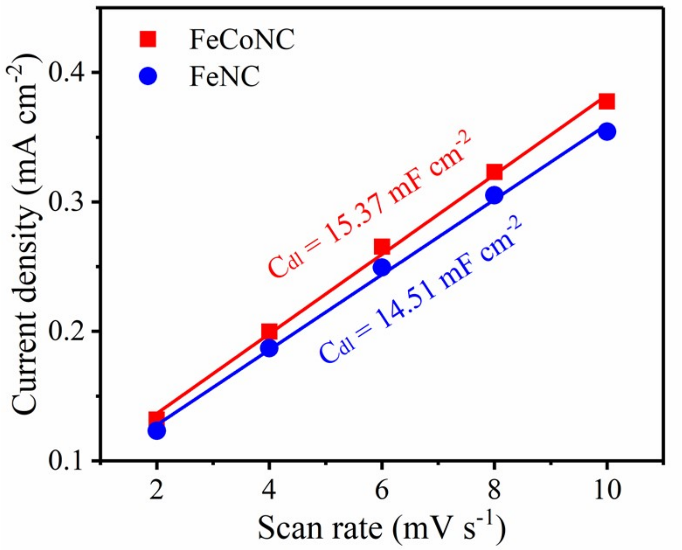

Fig. S8. Double-layer charging current plotted against the CV scan rate for FeCoNC and FeNC.

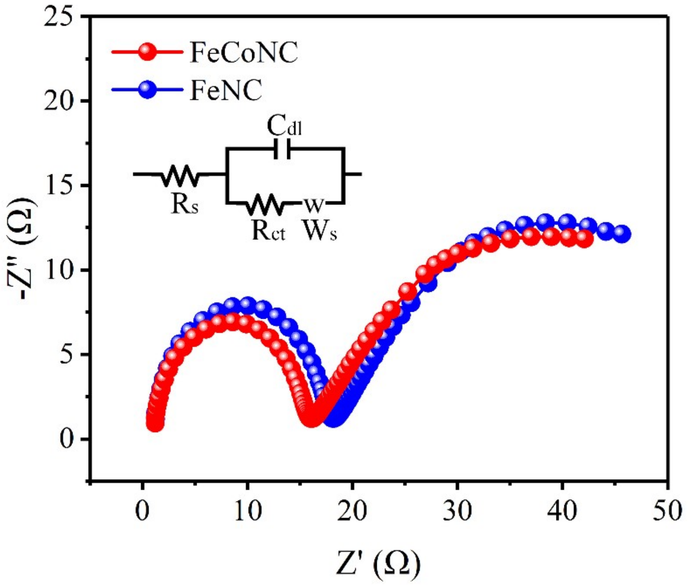

Fig. S9. Nyquist plots obtained using electrochemical impedance spectroscopy for the different electrodes, inset: the equivalent circuit used to fit the experiment data. Upon impedance spectra fitting, the charge transfer resistances (R_{ct}) are determined to be 14.6 Ω cm^{-2} for FeCoNC and 16.2 Ω cm^{-2} for FeNC.

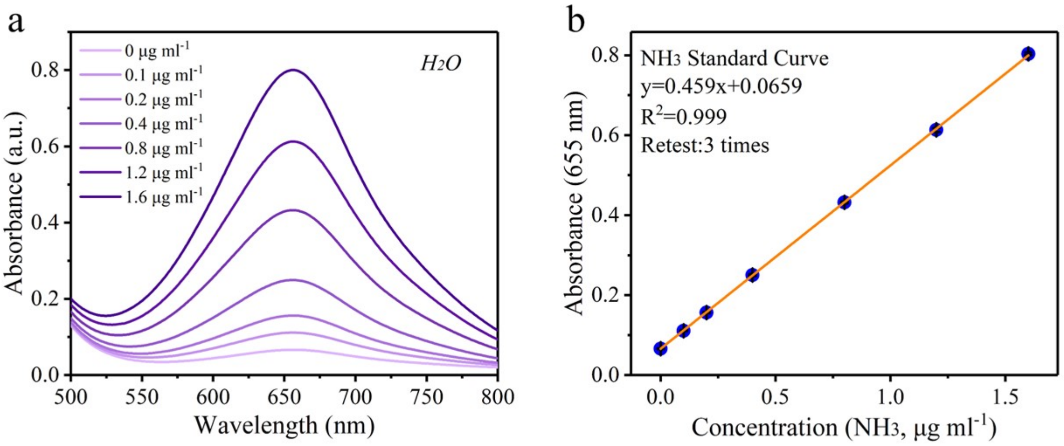

Fig. S10. (a) The UV-vis absorption spectra and (b) corresponding calibration curves for the colorimetric determination of NH_3 in ultrapure water using the indophenol blue method. The error bars correspond to the standard deviations of three separately prepared samples measured under identical conditions.

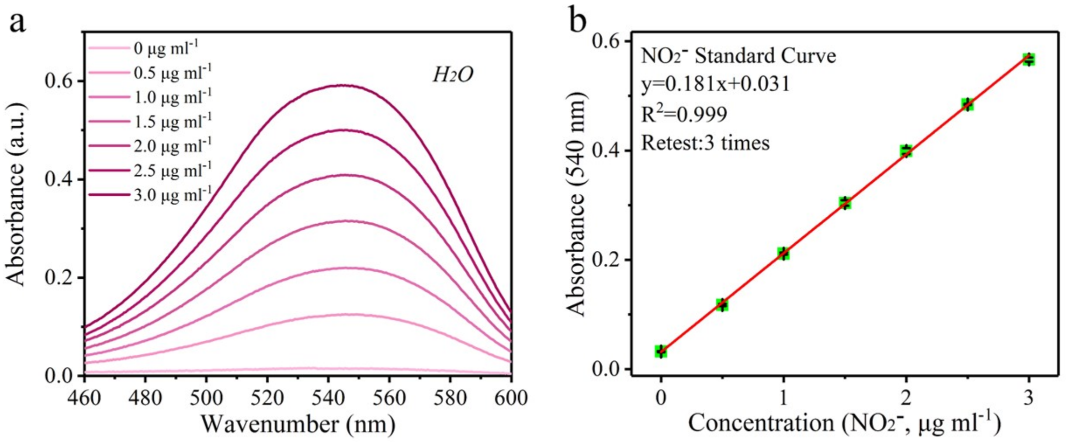

Fig. S11. (a) The UV-vis absorption spectra and (b) corresponding calibration curves for the colorimetric determination of NO_2^- in ultrapure water using the Griess spectrophotometric method. The error bars correspond to the standard deviations of three separately prepared samples measured under identical conditions.

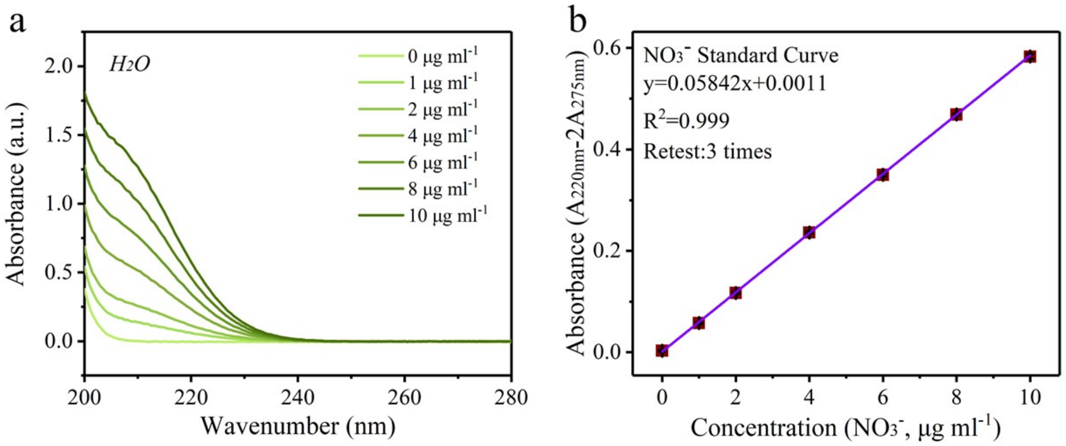

Fig. S12. (a) The UV-vis absorption spectra and (b) corresponding calibration curves for the colorimetric determination of NO_3^- in ultrapure water using the sulfamic acid spectrophotometric method in water. The error bars correspond to the standard deviations of three separately prepared samples measured under identical conditions.

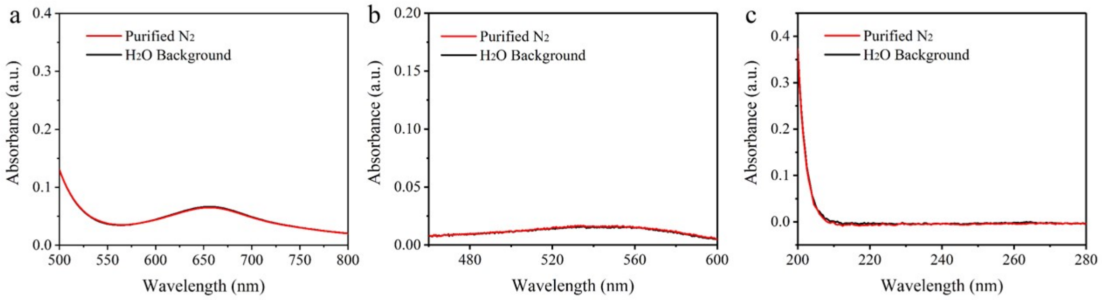

Fig. S13. The UV-vis absorption spectra of aqueous background and the purified N_2 treated water using (a) the indophenol blue method, (b) the Griess spectrophotometric method, and (c) the sulfamic acid spectrophotometric method.

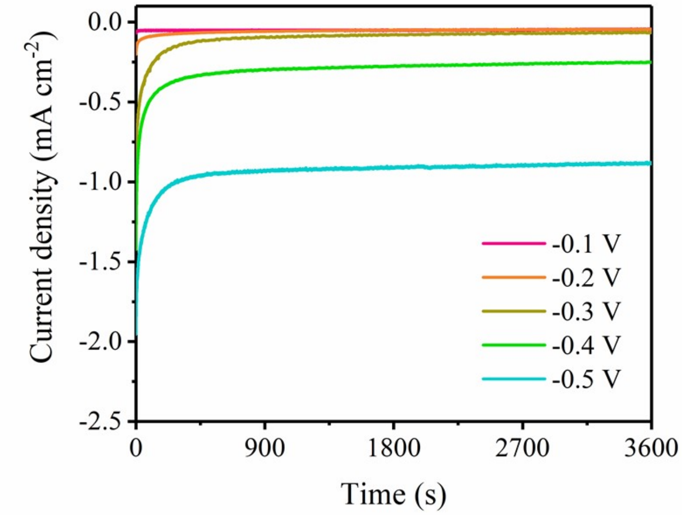

Fig. S14. Chronoamperometry results of FeNC tested in the H-cell with 0.1 M HCl at different applied potentials.

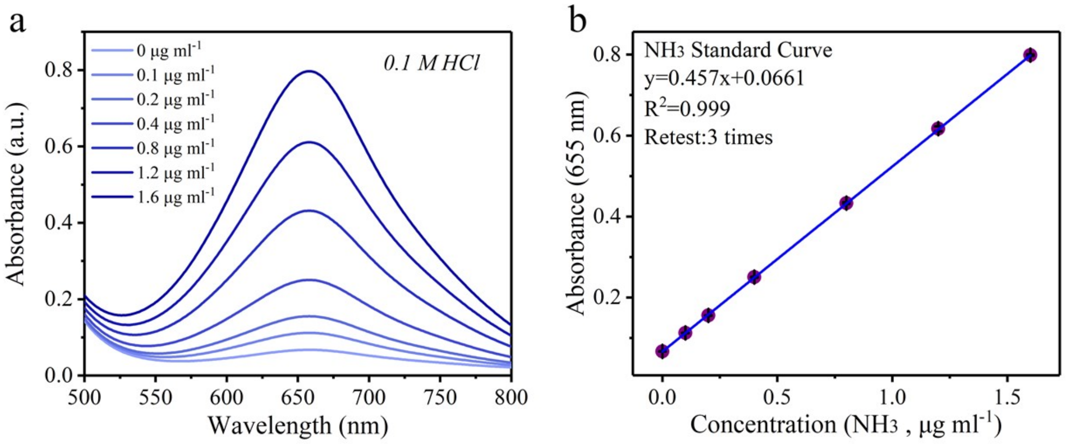

Fig. S15. (a) The UV-vis absorption spectra and (b) corresponding calibration curves for the colorimetric determination of NH_3 in 0.1 M HCl using the indophenol blue method. The error bars correspond to the standard deviations of three separately prepared samples measured under identical conditions.

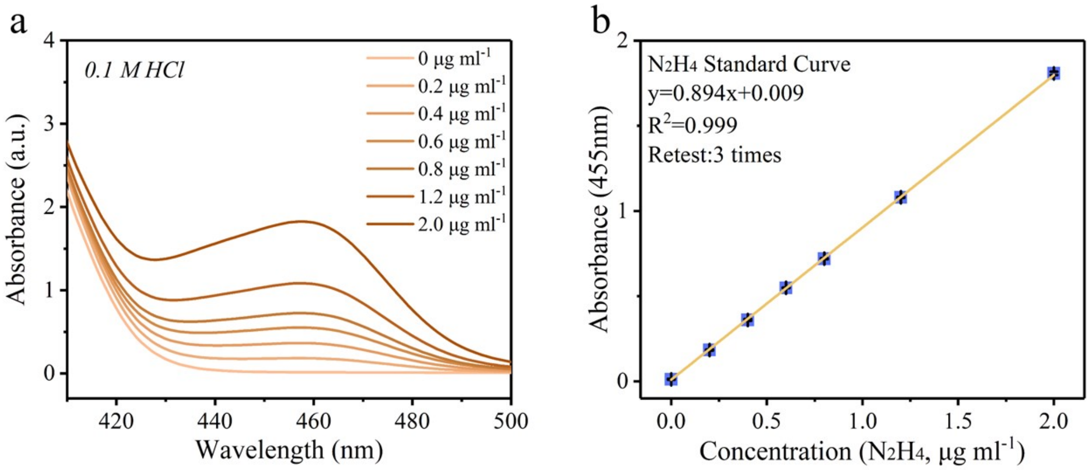

Fig. S16. (a) The UV-vis absorption spectra and (b) the corresponding calibration curves for colorimetric N_2H_4 determination in 0.1 M HCl using the Watt and Chrisp method. The error bars correspond to the standard deviations of three separately prepared samples measured under identical conditions.

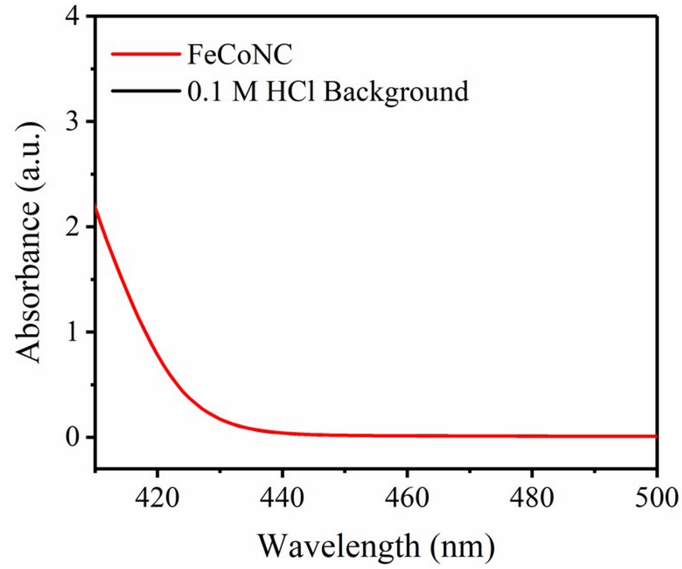

Fig. S17. The UV-vis absorption spectra of the electrolyte using the Watt and Chrisp method.

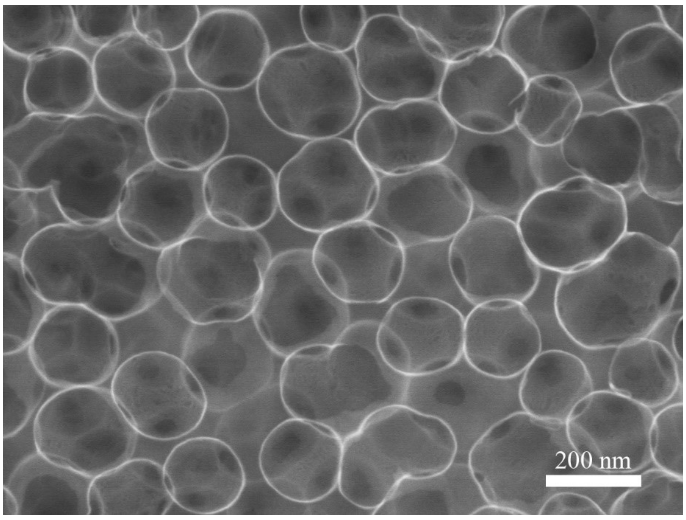

Fig. S18. Scanning electron microscopy image of FeCoNC after NRR electrolysis.

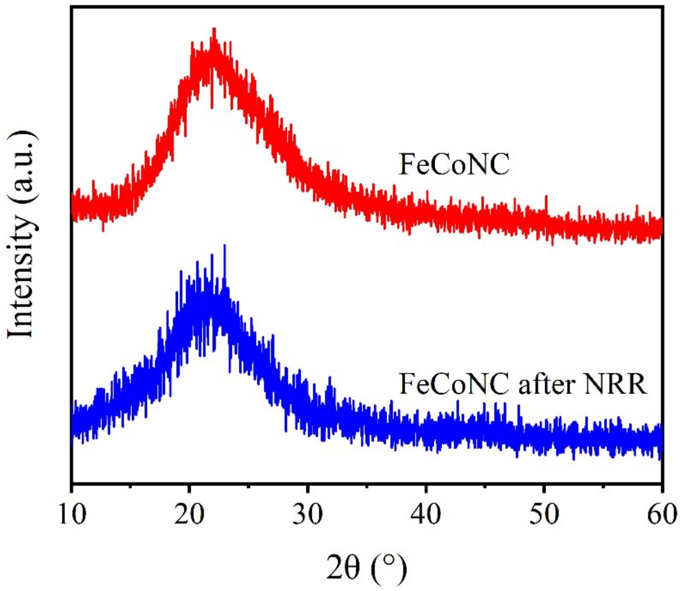

Fig. S19. XRD patterns of FeCoNC before and after NRR electrolysis.

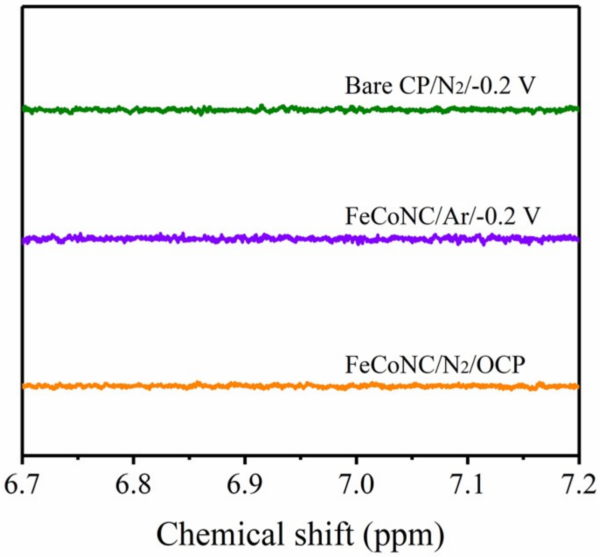

Fig. S20. ^{1}H NMR spectra of the electrolytes measured under different conditions.

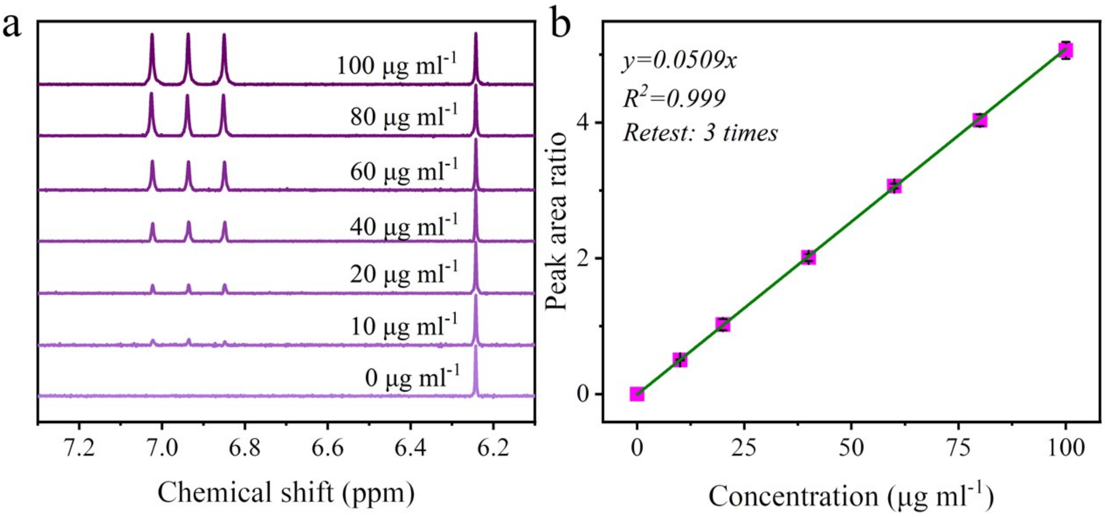

Fig. S21. (a) ^{1}H NMR spectra of different $^{14}NH_4^+$ concentrations. (b) Integral area ratio ($^{14}NH_4^+/C_4H_4O_4$) against $^{14}NH_4^+$ concentration. The error bars correspond to the standard deviations of three separately prepared samples measured under identical conditions.

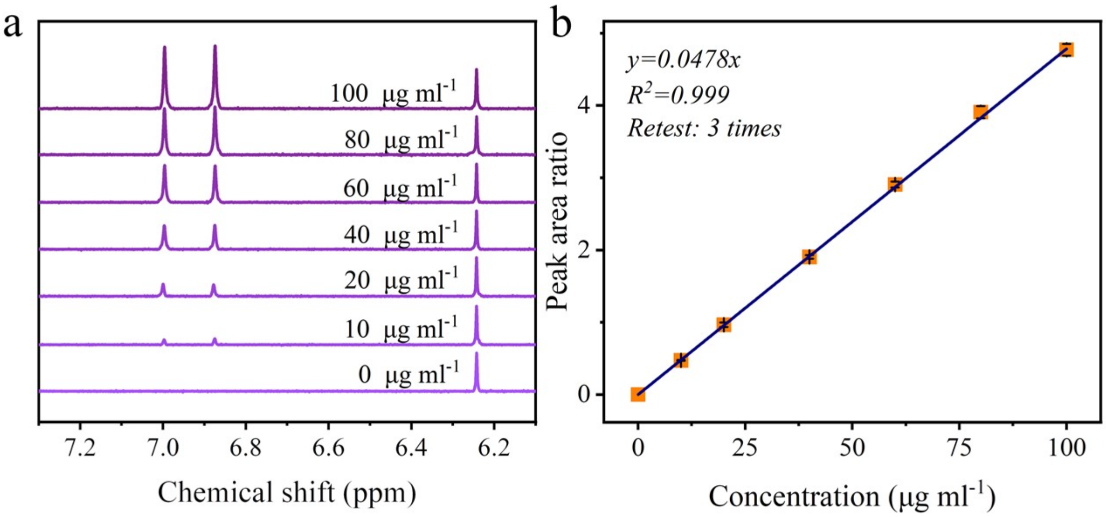

Fig. S22. (a) ^{1}H NMR spectra of different $^{15}NH_4^+$ concentrations. (b) Integral area ratio ($^{15}NH_4^+/C_4H_4O_4$) against $^{15}NH_4^+$ concentration. The error bars correspond to the standard deviations of three separately prepared samples measured under identical conditions.

Table S1. Comparison of the electrocatalytic NRR performance at ambient conditions.

Catalyst	**Electrolyte**	**Faradaic efficiency (%)**	**NH_3 yield rate (μg h^{-1} mg^{-1})**	**Ref.**
Non-noble metal-based catalysts				
FeCoNC	0.1 M HCl	32.16	70.11	**This work**
$Bi_4V_2O_{11}/CeO_2$	0.1 M HCl	10.16	23.21	1
Cr_2O_3 hollow microsphere	0.1 M Na_2SO_4	6.78	25.3	2
Cu/CN_x	0.1 M KOH	13.80	53.30	3
np-Mo_4P_3	0.1 M PBS	10.1	17.3	4
Zr^{4+}-doped anatase TiO_2	0.1 M KOH	17.30	8.90	5
Mo/FeS_2	0.1 M KOH	14.41	25.15	6
Fe-N/C-carbon nanotube	0.1 M KOH	9.28	34.83	7
$Ni_{0.75}Fe_{0.25}Se_2$	0.1 M Li_2SO_4	12.3	8.4	8
$BiVO_4$@MXene	0.1 M K_2SO_4	17.54	27.25	9
Noble metal-based catalysts				
Pd/C	0.1M PBS	8.2	4.5	10
Pd_3Pb nanowire networks	0.1 M Na_2SO_4	21.46	18.20	11
Au cluster/TiO_2	0.1 M HCl	8.11	21.40	12
Pd_3Cu_1	1 M KOH	1.2	39.9	13
$IrTe_4$	0.1 M KOH	14.4	26.2	14
Au-Fe_3O_4 Nanoparticles	0.1 M KOH	10.54	21.42	15
PdCu	0.5 M LiCl	11.50	35.70	16
PdRu nanorod	0.1 M HCl	2.40	34.20	17
Metal-free catalysts				
PEBCD	0.5 M Li_2SO_4	2.9	1.2	18
S-doped carbon nanosphere	0.1 M Na_2SO_4	7.47	19.07	19
Defect-rich fluorographene nanosheets	0.1 M Na_2SO_4	4.2	9.3	20
CN_xB_y	0.1 M HCl	10.58	16.40	21
NPC-500	0.005 M H_2SO_4	10.0	22.3	22
Metal-free polymeric carbon nitride	0.1 M HCl	11.59	8.09	23
B_4C	0.1 M HCl	16.0	26.6	24
Oxidized carbon nanotubes	0.1 M $LiClO_4$	12.50	32.33	25

Reference

1. C. Lv, C. Yan, G. Chen, Y. Ding, J. Sun, Y. Zhou and G. Yu, An amorphous noble-metal-free electrocatalyst that enables nitrogen fixation under ambient conditions, *Angew. Chem. Int. Ed.* 2018, **57**, 6073-6076.
2. Y. Zhang, W. Qiu, Y. Ma, Y. Luo, Z. Tian, G. Cui, F. Xie, L. Chen, T. Li and X. Sun, High-performance electrohydrogenation of N_2 to NH_3 catalyzed by multishelled hollow Cr_2O_3 microspheres under ambient conditions, *ACS Catal.* 2018, **8**, 8540-8544.
3. W. Zang, T. Yang, H. Zou, S. Xi, H. Zhang, X. Liu, Z. Kou, Y. Du, Y. Feng, L. Shen, L. Duan, J. Wang and S. J. Pennycook, Copper single atoms anchored in porous nitrogen-doped carbon as efficient pH-universal catalysts for the nitrogen reduction reaction, *ACS Catal.* 2019, **9**, 10166-10173.
4. L. Xiao, S. Zhu, Y. Liang, Z. Li, S. Wu, S. Luo, C. Chang and Z. Cui, Effects of hydrophobic layer on selective electrochemical nitrogen fixation of self-supporting nanoporous Mo_4P_3 catalyst under ambient conditions, *Appl. Catal. B-Environ.* 2021, **286**, 119895.
5. N. Cao, Z. Chen, K. Zang, J. Xu, J. Zhong, J. Luo, X. Xu and G. Zheng, Doping strain induced Bi-Ti^{3+} pairs for efficient N_2 activation and electrocatalytic fixation, *Nat. Commun.* 2019, **10**, 2877.
6. H.-B. Wang, J.-Q. Wang, R. Zhang, C.-Q. Cheng, K.-W. Qiu, Y.-J. Yang, J. Mao, H. Liu, M. Du, C.-K. Dong and X.-W. Du, Bionic Design of a Mo (IV)-doped FeS_2 catalyst for electroreduction of dinitrogen to ammonia, *ACS Catal.* 2020, **10**, 4914-4921.
7. Y. Wang, X. Cui, J. Zhao, G. Jia, L. Gu, Q. Zhang, L. Meng, Z, Shi, L. Zheng, C. Wang, Z. Zhang and W. Zheng, Rational design of Fe–N/C hybrid for enhanced nitrogen reduction electrocatalysis under ambient conditions in aqueous solution, *ACS Catal.* 2019, **9**, 336-344.
8. S. Yang, W. Ye, D. Zhang, X. Fang and D. Yan, Layered double hydroxide derived bimetallic nickel–iron selenide as an active electrocatalyst for nitrogen fixation under ambient conditions, *Inorg. Chem. Front.* 2021, **8**, 1762-1770.
9. D. Zhang, S. Yang, X. Fang, H. Li, X. Chen and D. Yan, In situ localization of $BiVO_4$ onto two-dimensional MXene promoting photoelectrochemical nitrogen reduction to ammonia, *Chinese Chem. Lett.* 2022, **33**, 4669-4674.
10. J. Wang, L. Yu, L. Hu, G. Chen, H. Xin and X. Feng, Ambient ammonia synthesis

via palladium-catalyzed electrohydrogenation of dinitrogen at low overpotential, *Nat. Commun.* 2018, **9**, 1795.

11. J. Guo, H. Wang, F. Xue, D. Yu, L. Zhang, S. Jiao, Y. Liu, Y. Lu, M. Liu, S. Ruan, Y.-J. Zeng, C. Ma and H. Huang, Tunable synthesis of multiply twinned intermetallic Pd_3Pb nanowire networks toward efficient N_2 to NH_3 conversion, *J. Mater. Chem. A* 2019, **7**, 20247-20253.
12. M.-M. Shi, D. Bao, B.-R. Wulan, Y.-H. Li, Y.-F. Zhang, J.-M. Yan and Q. Jiang, Au sub-nanoclusters on TiO_2 toward highly efficient and selective electrocatalyst for N_2 conversion to NH_3 at ambient conditions, *Adv. Mater.* 2017, **29**, 1606550.
13. F. Pang, Z. Wang, K. Zhang, J. He, W. Zhang, C. Guo and Y. Ding, Bimodal nanoporous Pd_3Cu_1 alloy with restrained hydrogen evolution for stable and high yield electrochemical nitrogen reduction, *Nano Energy* 2019, **58**, 834-841.
14. H. Wang, J. Wang, R. Zhang, C. Cheng, K. Qiu, Y. Yang, J. Mao, H. Liu, M. Du, C. Dong and X. Du, Bionic Design of a Mo(IV)-Doped FeS_2 Catalyst for Electroreduction of Dinitrogen to Ammonia, *ACS Catal.* 2020, **10**, 4914-4921.
15. J. Zhang, Y. Ji, P. Wang, Q. Shao, Y. Li and X. Huang, Adsorbing and activating N_2 on heterogeneous Au–Fe_3O_4 nanoparticles for N_2 fixation, *Adv. Funct. Mater.* 2019, **30**, 1906579.
16. W. Tong, B. Huang, P. Wang, L. Li, Q. Shao and X. Huang, Crystal-phase-engineered PdCu electrocatalyst for enhanced ammonia synthesis, *Angew. Chem. Int. Ed.* 2020, **59**, 2649-2653.
17. H. Wang, Y. Li, D. Yang, X. Qian, Z. Wang, Y. Xu, X. Li, H. Xue and L. Wang, Direct fabrication of Bi-metallic PdRu nanorod assemblies for electrochemical ammonia synthesis, *Nanoscale*, 2019, **11**, 5499-5505.
18. G. F. Chen, X. Cao, S. Wu, X. Zeng, L. X. Ding, M. Zhu and H. Wang, Ammonia electrosynthesis with high selectivity under ambient conditions via a Li^+ incorporation strategy, *J. Am. Chem. Soc.* 2017, **139**, 9771–9774.
19. L. Xi, X. Wu, Y. Wang, Z. Niu, Q. Liu, T. Li, X. Shi, A.M. Asiri and X. Sun, S-doped carbon nanospheres: an efficient electrocatalyst toward artificial N_2 fixation to NH_3, *Small Methods*, 2018, **3**, 1800251.
20. J. Zhao, J. Yang, L. Ji, H. Wang, H. Chen, Z. Niu, Q. Liu, T. Li, G. Cui and X. Sun, Defect-rich fluorographene nanosheets for artificial N_2 fixation under ambient conditions, *Chem. Commun.* 2019, **55**, 4266-4269.
21. J.-T. Ren, C.-Y. Wan, T.-Y. Pei, X.-W. Lv and Z.-Y. Yuan, Promotion of

electrocatalytic nitrogen reduction reaction on N-doped porous carbon with secondary heteroatoms, *Appl. Catal. B-Environ.* 2020, **266**, 118633.

22. C. Zhao, S. Zhang, M. Han, X. Zhang, Y. Liu, W. Li, C. Chen, G. Wang, H. Zhang and H. Zhao, Ambient electrosynthesis of ammonia on a biomass-derived nitrogen-doped porous carbon electrocatalyst: Contribution of pyridinic nitrogen, *ACS Energy Lett.* 2019, **4**, 377–383.
23. C. Lv, Y. Qian, C. Yan, Y. Ding, Y. Liu, G. Chen and G. Yu, Defect engineering metal-free polymeric carbon nitride electrocatalyst for effective nitrogen fixation under ambient conditions, *Angew. Chem. Int. Ed.* 2018, **57**, 10246-10250.
24. W. Qiu, X. Y. Xie, J. Qiu, W. H. Fang, R. Liang, X. Ren, X. Ji, G. Cui, A. M. Asiri, G. Cui, B. Tang and X. Sun, High-performance artificial nitrogen fixation at ambient conditions using a metal-free electrocatalyst, *Nat. Commun.* 2018, **9**, 3485.
25. J. Zhao, B. Wang, Q. Zhou, H. Wang, X. Li, H. Chen, Q. Wei, D. Wu, Y. Luo, J. You, F. Gong and X. Sun, Efficient electrohydrogenation of N_2 to NH_3 by oxidized carbon nanotubes under ambient conditions, *Chem. Commun.* 2019, **55**, 4997-5000.